

# Phosphorus in the Young Supernova Remnant Cassiopeia A

Bon-Chul Koo<sup>1\*</sup>, Yong-Hyun Lee<sup>1</sup>, Dae-Sik Moon<sup>2,3,4</sup>, Sung-Chul Yoon<sup>1</sup>  
& John C. Raymond<sup>5</sup>

<sup>1</sup>Department of Physics and Astronomy, Seoul National University,  
Seoul 151-747, Korea

<sup>2</sup>Department of Astronomy and Astrophysics, University of Toronto,  
Toronto, Ontario M5S 3H4, Canada

<sup>3</sup>Space Radiation Laboratory, California Institute of Technology,  
Pasadena, CA 91125, USA

<sup>4</sup>Visiting Brain Pool Scholar, Korea Astronomy and Space Science Institute,  
Daejeon 305-348, Korea

<sup>5</sup>Harvard-Smithsonian Center for Astrophysics,  
60 Garden Street, Cambridge, MA 02138, USA

**Phosphorus ( $^{31}\text{P}$ ), which is essential for life, is thought to be synthesized in massive stars and dispersed into interstellar space when these stars explode as supernovae (SNe). Here we report on near-infrared spectroscopic observations of the young SN remnant Cassiopeia A, which show that the abundance ratio of phosphorus to the major nucleosynthetic product iron ( $^{56}\text{Fe}$ ) in SN material is up to 100 times the average ratio of the Milky Way, confirming that phosphorus is produced in SNe. The observed range is compatible with predictions from SN nucleosynthetic models but not with the scenario in which the chemical elements in the inner SN layers are completely mixed by hydrodynamic instabilities during the explosion.**

Phosphorus (P) is an indispensable ingredient for life together with carbon, hydrogen, nitrogen, oxygen, and sulfur (S). In our solar system, its abundance relative to hydrogen is  $2.8 \times 10^{-7}$  by number, which is 50 to 1900 times less than those of the other life-keeping  $\alpha$  elements (1). The abundance of P in the diffuse interstellar medium and stars in our galaxy's disk is comparable with that of the solar system or the cosmic abundance, with some dependence on metallicity (2, 3). P is believed to be mainly formed in massive [ $\gtrsim 8 M_{\odot}$ ] stars by neutron capture on silicon (Si) in hydrostatic neon-burning shells in the pre-SN stage and also in explosive carbon and neon burning layers during SN explosion (4, 5).

Freshly synthesized P should thus be found in young core-collapse SN remnants (SNRs) resulting from the explosion of massive stars. Cassiopeia A (Cas A) is the youngest confirmed core-collapse SNR in our galaxy; it has been extensively studied in all wavebands (Fig. 1). It is located at a distance of 3.4 kpc (6) and thought to be the remnant of a SN event in C.E.  $1681 \pm 19$  (7). The spectrum of the light echo from the SN event indicated a SN of Type IIb that had a small hydrogen envelope at the time of explosion (8). The total estimated mass of the SN ejecta is 2 to  $4 M_{\odot}$ , and the inferred initial mass of the progenitor star ranges from 15 to  $25 M_{\odot}$  (9, 10). Emission from P II was previously detected from Cas A (11), but no analysis of the emission line has been done.

We conducted near-infrared (NIR) spectroscopic observations of the main SN ejecta shell using the TripleSpec spectrograph mounted on the Palomar 5-m Hale telescope in 2008 (Fig. 1) (12). TripleSpec provides continuous wavelength coverage from 0.94 to  $2.46 \mu\text{m}$  at medium spectral resolving power of  $\sim 2,700$ . By analyzing the spectra, we identified 63 knots of emission and, for each knot, measured the radial velocities and fluxes of emission lines, including [P II] lines (12).

The knots show distinct spectroscopic and kinematic properties depending on their origins (Fig. 2). The knots with strong [S II] lines (Fig. 2, red symbols) have high ( $\gtrsim 100 \text{ km s}^{-1}$ )

radial velocities, and most of them have strong [P II] lines too, suggesting that the production of P is tightly correlated with the production of S. Some knots without apparent [S II] lines have low radial velocities ( $\lesssim 100 \text{ km s}^{-1}$ ) and strong He I lines (Fig. 2, green symbols). Their properties match those of “quasi-stationary flocculi”, the material lost from the hydrogen envelope of the progenitor during its red-supergiant phase as slow wind (13, 14). The rest of the knots without [S II] lines (Fig. 2, blue symbols) have little He I emission, and most of them have high radial velocities. They have [Fe II] lines as strong as those from the other knots. These knots are probably pure iron (Fe) material from complete Si-burning in the innermost region of the SN, corresponding to the pure Fe ejecta detected in x-rays (9). They are found mainly in the southern bright [Fe II] filament, where the x-ray-emitting Fe ejecta is not prominent (Fig. 1).

The P/Fe abundance ratio of the knots can be derived from the flux ratio of [P II] 1.189  $\mu\text{m}$  and [Fe II] 1.257  $\mu\text{m}$  lines ( $F_{[\text{P II}]1.189}/F_{[\text{Fe II}]1.257}$ ). These two lines have comparable excitation energies and critical densities, which together with the fact that the ionization energies of P and Fe are comparable (10.49 and 7.90 eV) greatly simplifies the abundance analysis (15). (This is not the case for [S II] lines that have considerably higher excitation energies.) We assume that the line-emitting region is at  $T_e = 10,000 \text{ K}$  and has a uniform density, with equal fractions of singly ionized ions. This simple model yields P/Fe abundances accurate to within  $\sim 30\%$  mostly for both SN and circumstellar knots (12). The observed  $F_{[\text{P II}]1.189}/F_{[\text{Fe II}]1.257}$  ratios (Fig. 3) imply that the P-to-Fe abundance ratio by number,  $X(\text{P}/\text{Fe})$ , of the SN ejecta knots is up to 100 times higher than the cosmic abundance  $X_{\odot}(\text{P}/\text{Fe}) = 8.1 \times 10^{-3}$  (1), whereas the knots of the circumstellar medium have ratios close to the cosmic abundance. The enhanced P abundance over Fe in these SN ejecta knots is direct evidence for the in situ production of P in Cas A.

The observed range of  $X(\text{P}/\text{Fe})$  is compatible with the local nucleosynthetic yield of P in SN models. The internal chemical composition and the resulting  $X(\text{P}/\text{Fe})$  profile of a spher-

ically symmetric SN model for progenitor mass of  $15 M_{\odot}$  is shown in Fig. 4 (16). In the oxygen-rich layer, P is enhanced, whereas Fe is slightly depleted because of neutron capture. ( $^{56}\text{Fe}$  and  $^{58}\text{Fe}$  are the two major Fe isotopes in the oxygen-rich layer.) This makes  $X(\text{P}/\text{Fe})$  higher by two orders of magnitude than that of the outer He-rich layer, which is essentially equal to the cosmic abundance. The extended P enhancement in  $M/M_{\text{core}} = 0.55$  to  $0.73$  is the result of hydrostatic burning in pre-SN, whereas the bump at  $M/M_{\text{core}} \sim 0.5$  is due to explosive burning during the explosion. The knots that we observed are probably from somewhere in the oxygen-rich layer. It is, however, difficult to precisely determine the knots' original positions in the progenitor star from the comparison of the measured P/Fe ratio with the model prediction because the local  $X(\text{P}/\text{Fe})$  are very much model-dependent (Fig. 4B) and subject to further modifications owing to the Rayleigh-Taylor instability during the explosion (17). We instead assumed that the knots have been expanding freely, with an expansion rate of  $2800 \text{ km s}^{-1} \text{ pc}^{-1}$  (18). We then converted the obtained space velocities to mass coordinates using the ejecta velocity profile of a  $15 M_{\odot}$  SN IIB model (19) scaled to the chemical structure of the model in Fig. 4 (16). The resulting mass coordinates have considerable uncertainties because of model-dependency but provide rough locations of the knots (Fig. 4B).

$X(\text{P}/\text{Fe})$  of the [P II] line-emitting ejecta knots fall into the  $X(\text{P}/\text{Fe})$  range of the oxygen-rich layer in the model, whereas the  $X(\text{P}/\text{Fe})$  of the “pure” Fe knots are often less than the cosmic abundance (Fig. 4B). The fact that the circumstellar knots have  $X(\text{P}/\text{Fe})$  close to the cosmic abundance— $X(\text{P}/\text{Fe}) \sim 2X_{\odot}(\text{P}/\text{Fe})$ —gives confidence in the derived  $X(\text{P}/\text{Fe})$  in the core. The extended  $X(\text{P}/\text{Fe})$  range over nearly two orders of magnitude may be explained by the hydrodynamic chemical mixing during the SN explosion. But, our result does not support a complete mixing of the core below the He-rich layer because in such a case,  $X(\text{P}/\text{Fe})$  will be much lower as marked by the brown arrow in Fig. 4B; the available yields in the literature imply  $X(\text{P}/\text{Fe})=0.01$  to  $0.05$  for a SN of  $15$  to  $25 M_{\odot}$  (4, 16, 20, 21), which is represented by

the solid part of the arrow, or 0.01 to 0.15 when the unusually high P yield of the  $20 M_{\odot}$  model of (16) is included. The detection of P-depleted, pure Fe material probably produced in the innermost, complete Si-burning layer also indicates that these dense SN ejecta materials largely retain their original abundance.

The high  $X(\text{P}/\text{Fe})$  ratio, in principle, could also result from the depletion of Fe in the gas phase if Fe atoms are locked in dust grains. In Cas A, a substantial amount ( $\sim 0.1 M_{\odot}$ ) of newly formed dust grains in the SN ejecta has been indeed detected (22–24). But, they are most likely silicate dust, with only 1% of Fe in the form of FeS (25). Also, the fact that [P II] lines in the SN ejecta are much stronger than in the circumstellar knots (Fig. 2) is best explained by the enhanced abundance of P rather than by the depletion of Fe onto dust.

## References and Notes

1. M. Asplund, N. Grevesse, A. J. Sauval & P. Scott, *Annu. Rev. Astron. Astrophys.*, **47**, 481 (2009)
2. V. Leboutteiller, Kuassivi & R. Ferlet, *Astron. Astrophys.*, **443**, 509 (2005)
3. E. Caffau, P. Bonifacio, R. Faraggiana & M. Steffen, *Astron. Astrophys.*, **532**, A98 (2011)
4. S. E. Woosley & T. A. Weaver, *Astrophys. J. Suppl. S.*, **101**, 181 (1995)
5. Another type of stellar explosions (Type Ia supernovae) are also thought to contribute but to a much lesser extent (26, 27).
6. J. E. Reed, J. J. Hester, A. C. Fabian & P. F. Winkler, *Astrophys. J.*, **440**, 706 (1995)
7. R. A. Fesen, M. C. Hammell, J. Morse *et al.*, *Astrophys. J.*, **645**, 283 (2006)
8. O. Krause, S. M. Birkmann, T. Usuda *et al.*, *Science*, **320**, 1195 (2008)

9. U. Hwang & J. M. Laming, *Astrophys. J.*, **746**, 130 (2012)
10. P. A. Young, C. L. Fryer, A. Hungerford *et al.*, *Astrophys. J.*, **640**, 891 (2006)
11. C. L. Gerardy & R. A. Fesen, *Astron. J.*, **121**, 2781 (2001)
12. Materials and methods are available as supplementary materials on *Science Online*.
13. S. van den Bergh, *Astrophys. J.*, **165**, 457 (1971)
14. J.-J. Lee, S. Park, J. P. Hughes & P. O. Slane, arXiv:1304.3973 (2013)
15. E. Oliva, A. Marconi, R. Maiolino *et al.*, *Astron. Astrophys.*, **369**, L5 (2001)
16. T. Rauscher, A. Heger, R. D. Hoffman & S. E. Woosley, *Astrophys. J.*, **576**, 323 (2002)
17. K. Kifonidis, T. Plewa, H.-T. Janka & E. Müller, *Astron. Astrophys.*, **408**, 621 (2003)
18. T. DeLaney, L. Rudnick, M. D. Stage *et al.*, *Astrophys. J.*, **725**, 2038 (2010)
19. S. E. Woosley, R. G. Eastman, T. A. Weaver, & P. A. Pinto, *Astrophys. J.*, **429**, 300 (1994)
20. C. Kobayashi, H. Umeda, K. Nomoto, K. *et al.*, *Astrophys. J.*, **653**, 1145 (2006)
21. A. Chieffi & M. Limongi, *Astrophys. J.*, **764**, 21 (2013)
22. J. Rho, T. Kozasa, W. T. Reach *et al.*, *Astrophys. J.*, **673**, 271 (2008)
23. B. Sibthorpe, P. A. R. Ade, J. J. Bock *et al.* *Astrophys. J.*, **719**, 1553 (2010)
24. M. J. Barlow, O. Krause, B. M. Swinyard *et al.* *Astron. Astrophys.*, **518**, L138 (2010)
25. T. Nozawa, T. Kozasa, N. Tominaga *et al.*, *Astrophys. J.*, **713**, 356 (2010)
26. G. Cescutti, F. Matteucci, E. Caffau & P. François, *Astron. Astrophys.*, **540**, A33 (2012)

27. C. West & A. Heger, *Astrophys. J.*, **774**, 75 (2013)

28. J. R. Thorstensen, R. A. Fesen & S. van den Bergh, *Astron. J.*, **122**, 297 (2001)

**Acknowledgements:** This work was supported by Basic Science Research (NRF-2011-0007223) and International Cooperation in Science and Technology (NRF-2010-616-C00020) programs through the National Research Foundation of Korea (NRF) funded by the Ministry of Education, Science and Technology, and also by the Korean Federation of Science and Technology Societies (KOFST). D.-S. M. acknowledges support from the the Natural Science and Engineering Research Council of Canada. We thank M. Munro for his help in observations and J.-J. Lee for providing the *Chandra* 1Ms x-ray images.

### **Supplementary Materials**

[www.sciencemag.org/cgi/content/full/science.1243823/DC1](http://www.sciencemag.org/cgi/content/full/science.1243823/DC1)

Materials and Methods

Figs. S1 to S4

Tables S1 to S2

References (29–49)

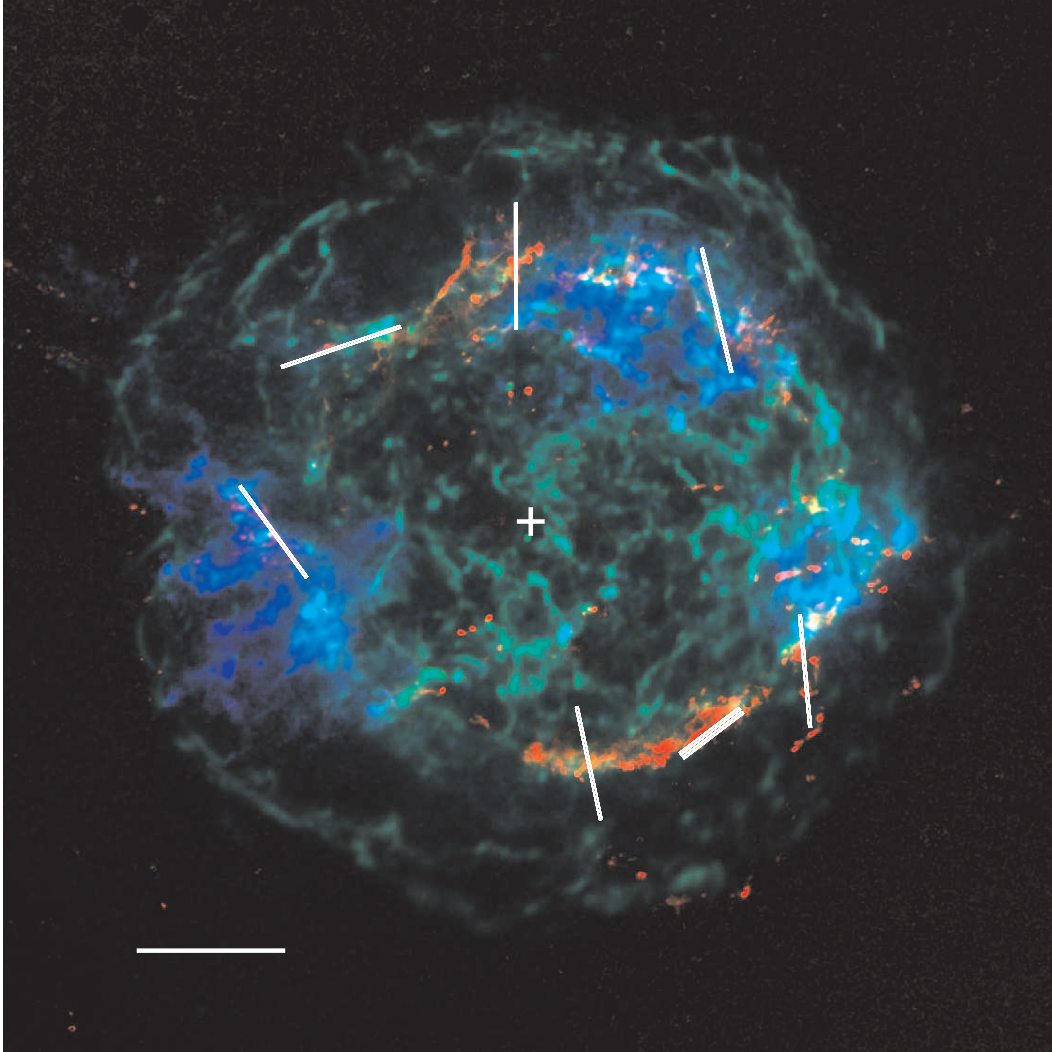


Figure 1: **Fig. 1. Three-color composite image of the young supernova remnant Cas A.** Red is a Palomar [Fe II] 1.644- $\mu\text{m}$  image representing SN material at  $\sim 10^4$  K, green is a *Chandra* x-ray continuum (4.20 to 6.40 keV) image representing hot gas and relativistic particles that are heated by SNR blast wave, and blue is a *Chandra* Fe K (6.52 to 6.94 keV) image representing SN material at  $\sim 2 \times 10^7$  K, respectively. The slit positions in our NIR spectroscopic observations are marked by thin white bars. The central white plus symbol represents the position of the SN explosion center determined from proper motions (28). The scale bar in the lower left represents an angular scale of  $1'$ , which corresponds to 1 pc at the distance (3.4 kpc) of the SNR.



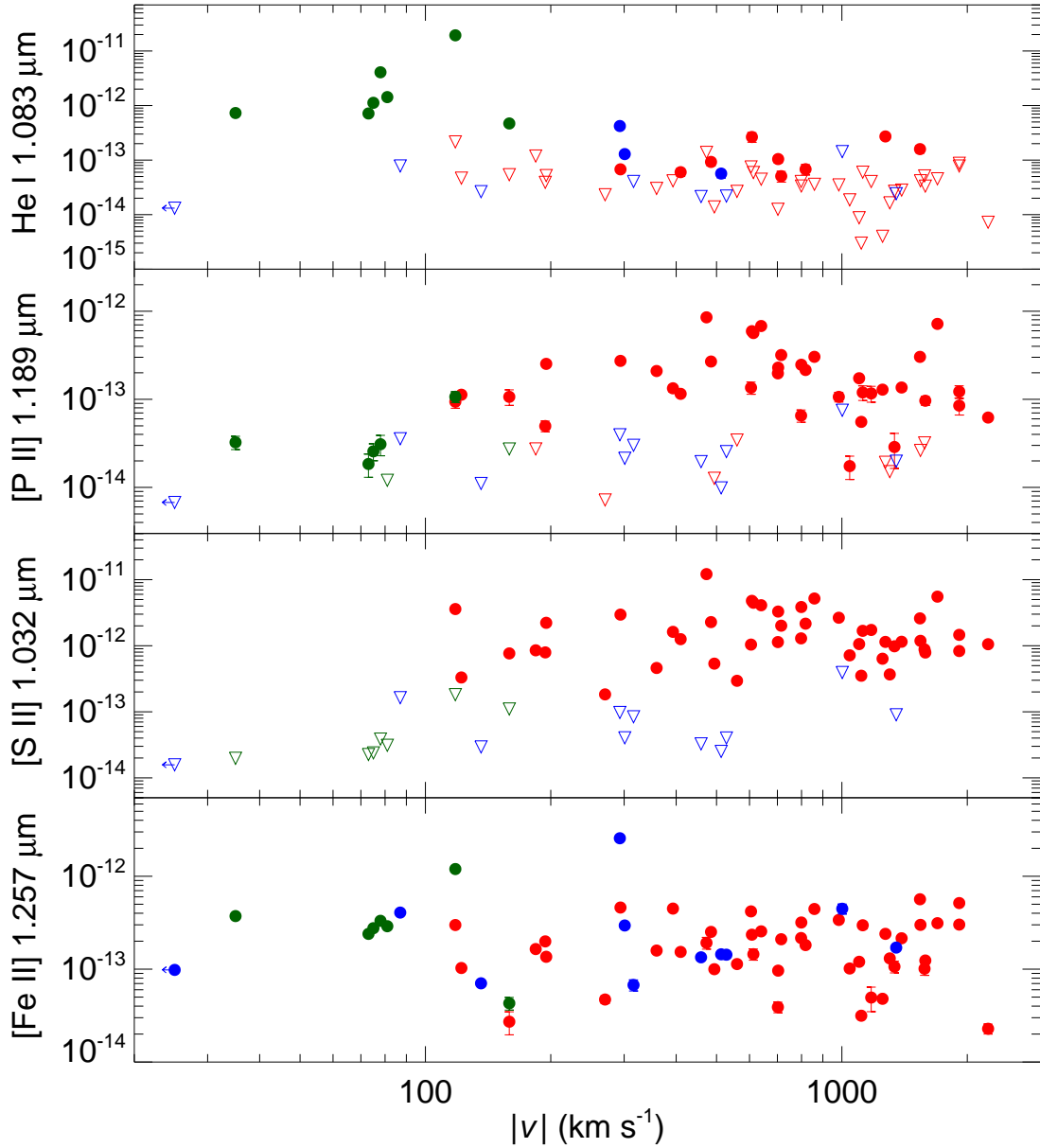


Figure 2: **Fig. 2. NIR line fluxes of the Cas A's knots as a function of their radial velocities.** NIR line fluxes are in erg per square centimeter per second. Shown are He I  $1.083 \mu\text{m}$  ( $^3P \rightarrow ^3S_1$ ), [P II]  $1.189 \mu\text{m}$  ( $^1D_2 \rightarrow ^3P_2$ ), [S II]  $1.032 \mu\text{m}$  ( $^2P_{3/2} \rightarrow ^2D_{5/2}$ ), and [Fe II]  $1.257 \mu\text{m}$  ( $a^4D_{7/2} \rightarrow a^6D_{9/2}$ ) lines from top to bottom. The knots not detected in the line emission are marked by open, upside-down triangles representing  $3\sigma$  upper limits. The fluxes are corrected for extinction. The different colors represent knots of different characteristics: red symbols, knots with strong [S II] lines; green symbols, knots without [S II] lines but with strong He I lines at low radial velocities ( $\lesssim 100 \text{ km s}^{-1}$ ); blue symbols, knots without [S II] lines and with little He I emission

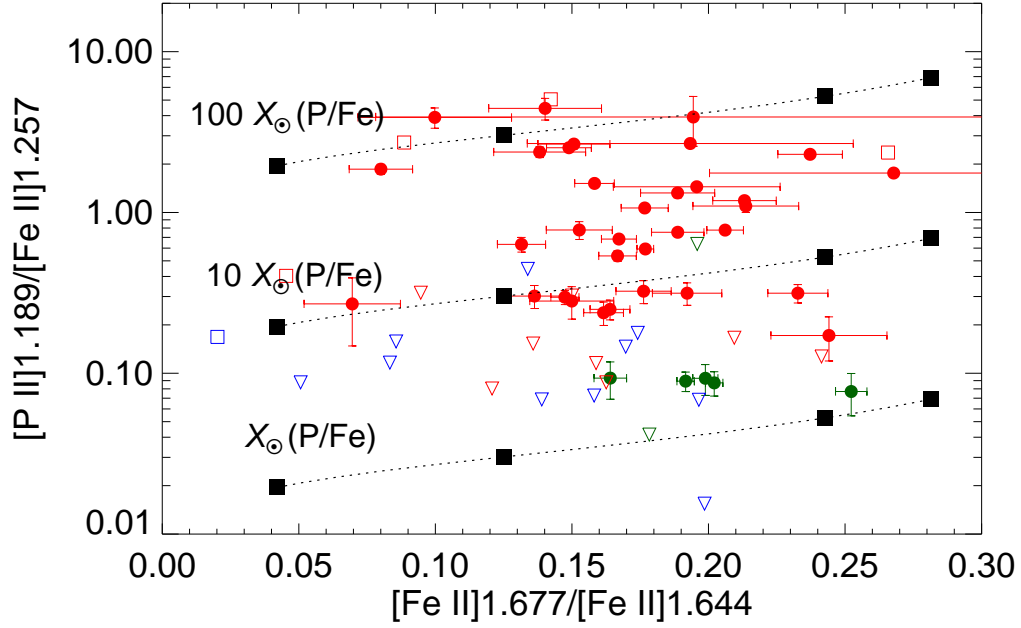


Figure 3: **Fig. 3. [P II] 1.189/[Fe II] 1.257 versus density-sensitive [Fe II] line ratios of the Cas A's knots.** The knots are marked in the same colors as in Fig. 2. The open, upside-down triangles represent the knots undetected in the [P II] line emission, whereas the open squares represent the knots undetected in [Fe II] 1.677  $\mu\text{m}$  line emission including the one undetected in either line emission at (0.020, 0.17). The dotted lines show theoretical line ratios for  $X(\text{P}/\text{Fe})=1$ , 10, and 100 times the cosmic abundance. The solid squares along the lines represent the ratios at  $n_e = 10^3, 10^4, 10^5$ , and  $10^6 \text{ cm}^{-3}$  from left to right. The [Fe II] line ratio in the abscissa is essentially given by a function of  $n_e$ , and the observed ratios indicate that  $n_e = 3 \times 10^3$  to  $2 \times 10^5 \text{ cm}^{-3}$ .

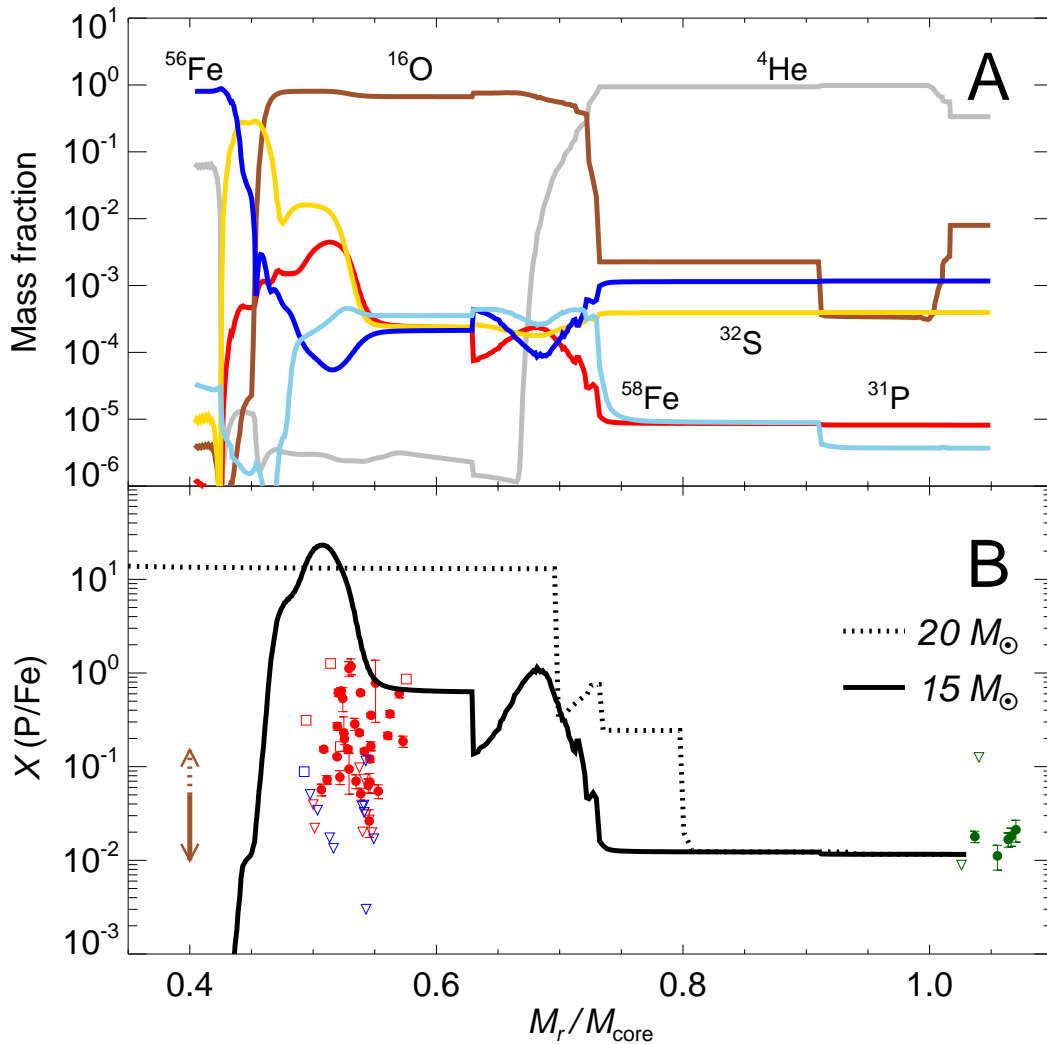


Figure 4: **Fig. 4. Comparison of the abundance ratio  $X(\text{P}/\text{Fe})$  of the Cas A's knots with predictions from SN nucleosynthetic models.** (A) Internal, post-SN chemical composition of a  $15 M_{\odot}$  SN model (16). The abscissa is the mass inside a radius  $r$  from the explosion center normalized by the mass of the SN core which is  $4.163 M_{\odot}$ . The mass inside the “mass cut” ( $1.683 M_{\odot}$  or  $M_r/M_{\text{core}} = 0.40$ ) becomes a stellar remnant, whereas the rest is ejected with the explosion. Most of the mass outside the core would have been lost as a stellar wind for SN Type IIb such as Cas A. In a real SN, the profile will be smoother because of the hydrodynamic mixing of material. (B) Profile of the abundance ratio  $X(\text{P}/\text{Fe})$  of the  $15 M_{\odot}$  SN (solid line). The Fe abundance includes all stable Fe isotopes. The observed  $X(\text{P}/\text{Fe})$  ratios of the Cas A SN ejecta knots are marked in the same colors and symbols as in Fig. 3. The knots of circumstellar medium (green symbols) are marked at  $M_r/M_{\text{core}} > 1$ . For comparison, the dotted line shows  $X(\text{P}/\text{Fe})$  profile of a  $20 M_{\odot}$  SN (16) with a very high P yield because of unusual convection mixing the Si and oxygen layers before the explosion. The other typical SN models of 15 to  $25 M_{\odot}$  in the literature have chemical structures similar to that of the  $15 M_{\odot}$  SN model here. The brown arrow to the left represents the expected range of  $X(\text{P}/\text{Fe})$  for a complete mixing of the core below the He-rich layer.

## Supplementary Materials

### S1. Observation and data reduction

The near-infrared (NIR) spectroscopic observations of Cassiopeia A (Cas A) were carried out with the TripleSpec spectrograph mounted on the 5-m Palomar Hale telescope on June 29 and August 8, 2008. TripleSpec is a slit-based NIR cross-dispersion echelle spectrograph covering the entire NIR atmospheric windows simultaneously with a spectral resolving power  $R \approx 2500$ – $3000$  (29, 30). The slit width and length of TripleSpec are  $1''$  and  $30''$ , respectively. We obtained spectra at eight slit positions well spread over the bright, main shell of Cas A (see Fig. 1 in the Report). At each position, reference background spectra were obtained either within the slit, by observing the target at the two nod positions at  $1/3$  (A) and  $2/3$  (B) locations along the slit in an ABBA pattern, e.g., see (31), or outside the slit if the field was too crowded to obtain useful background spectra within the slit. The background spectra were then subtracted out. In Fig. 1, the positions represented by long ( $45''$ ) white bars are where the spectra were obtained in the ABBA pattern, while the positions represented by the  $30''$ -long white bars are where the reference spectra were obtained outside the slit. The total exposure time per slit ranged from 300 sec to 1,800 sec.

For the data reduction, we followed the standard procedure of pre-processing including dark subtraction, flat-fielding correction, and bad pixel removal. We then obtained wavelength solutions using the OH airglow emission lines in the band, and corrected the wavelength to the heliocentric reference frame. The sky background including OH lines were subtracted out as much as possible

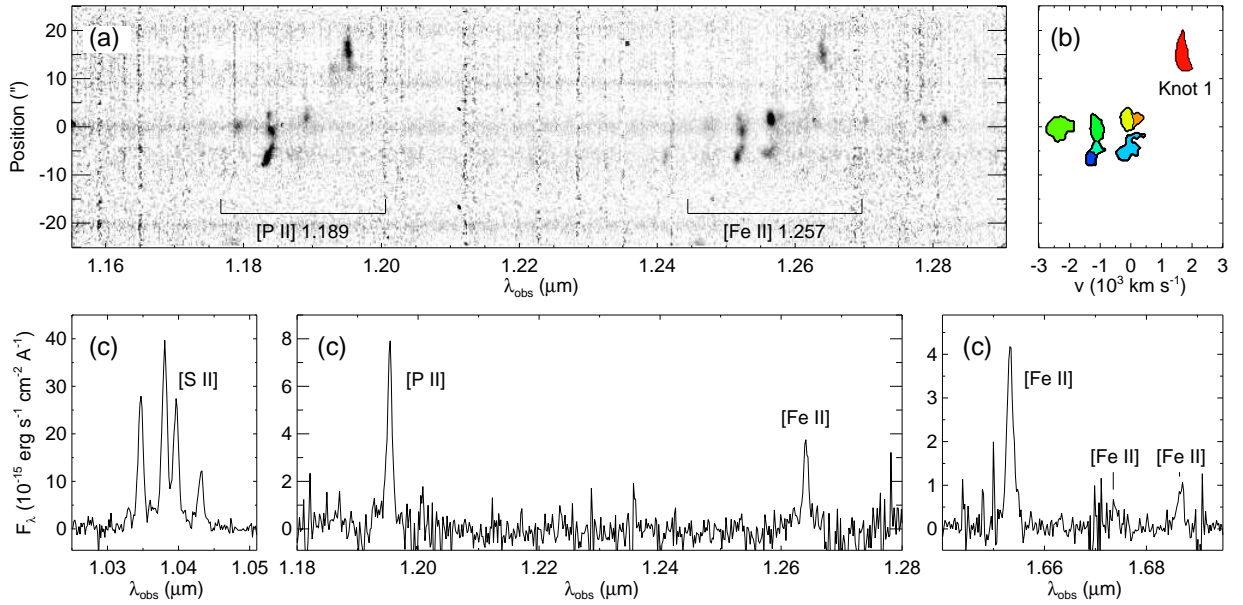


Figure S1: (a) Portion of the two-dimensional dispersed image of Slit 1 showing [P II] 1.189  $\mu\text{m}$  and [Fe II] 1.257  $\mu\text{m}$  lines. (b) Color-coded ‘mask image’ showing the areas in the two-dimensional dispersed image occupied by individual knots identified from the *Clumpfind* routine (32). The abscissa is the radial velocity determined from the Doppler shifts of the lines. (c) One dimensional spectrum of Knot 1 extracted from (a) using the mask in (b).

using the dithered or background frames. The flux calibration was done by comparing the spectra of the nearby A0V standard star (HD 223386) observed just before or after the target observations to the Kuruz model spectrum. We estimate a systematic uncertainty of 30% in the absolute flux, but this uncertainty did not enter into the analysis of relative abundances.

Along a slit, there are usually several [Fe II]-line emitting filaments or knots of distinct kinetic properties, so that, in a two-dimensional dispersed image, we observe complex emission

features distributed along both the space and velocity (or wavelength) dimensions. For example, Fig. S1 (a) shows a portion of the processed dispersed image of Slit 1, where we see more than five distinct “knots” emitting both [P II] 1.189 and [Fe II] 1.257  $\mu\text{m}$  lines. In order to study the physical conditions of the emitting regions, we first need to separate out individual emission features. We used the clump-finding algorithm *Clumpfind* (32), which is developed for the identification of clumps in molecular clouds. Using a set of contour levels provided as an input parameter, the routine searches local maxima, decomposes clumps, and determines their locations and sizes. We used a set of contour levels starting at  $2\sigma$  of the background RMS noise with a  $2\sigma$  increment. The identification has been made in the dispersed image of the [Fe II] 1.644  $\mu\text{m}$  line which is essentially identical to that of the [Fe II] 1.257  $\mu\text{m}$  line in Fig. S1(a). If the [Fe II] line is weaker than the [S III] 0.953  $\mu\text{m}$  or [P II] 1.189  $\mu\text{m}$  lines, we used the latter. Fig. S1 (b) shows the result of applying *Clumpfind* to Slit 1, which yielded eight knots in total. These “masks” in dispersed images are then used to extract one-dimensional spectra of the knots. Fig. S1 (c) shows the extracted one-dimensional spectrum of Knot 1. The line fluxes are derived from Gaussian least-squares fittings of the spectra.

The derived line parameters of the five emission lines used in our analysis are listed in Table S1. The radial velocities are those of [Fe II] 1.257  $\mu\text{m}$  lines, which agree with those of the other lines within about  $100 \text{ km s}^{-1}$ , comparable with the spectral resolution of our data. Note that the line fluxes are extinction corrected based on the ratio of [Fe II] 1.257 and 1.644  $\mu\text{m}$  lines. Since these two lines share the same upper level ( $a^4 D_{7/2}$ ) (see the next section), their line ratio is determined by the ratio of  $A_{21}\nu_{21}$  where  $A_{21}$  is Einstein  $A$  coefficients for spontaneous transition

from the upper (2) to the lower (1) state and  $\nu_{21}$  is the frequency of the line. We adopt the recent theoretical result of (33), which gives the intrinsic ratio  $F_{1.257}/F_{1.644} = 1.36$ . The deviation of the observed line ratio from this is due to the extinction, and the corresponding corrections are applied to the other lines using the extinction curve of the carbonaceous-silicate grain model with Milky Way size distribution for  $R_V = 3.1$  (34).

We note that there is a weak [Fe II] line at  $1.18848 \mu\text{m}$  ( $a^2G_{7/2} \rightarrow a^4D_{7/2}$ ) that overlaps with [P II]  $1.189$  ( $1.18861$ )  $\mu\text{m}$  line. Its expected intensity relative to the [Fe II]  $1.257 \mu\text{m}$  line is  $\lesssim 10^{-5}$  at the electron densities  $\lesssim 10^5 \text{ cm}^{-3}$ , and consequently its contribution to the [P II] line flux should be negligible. The identification of this line reported in previous studies (11, 35) is most likely a misidentification of the [P II] line.

## S2. Abundance analysis of [P II] and [Fe II] emission lines

In this section, we describe the basic properties of the forbidden lines that we use in our analysis and how we analyze them to derive the abundance ratios.

### Near-infrared forbidden lines of $\text{P}^+$ and $\text{Fe}^+$

The lines that we use in our analysis are the forbidden lines from P II and Fe II. The energy level diagrams of the ground terms of these ions are shown in Fig. S2. P II is a  $p^2$ -ion and has three low-lying terms. The ground term ( $^3P$ ) is split into three fine-structure levels, and the transition from  $^1D_2$  to these levels produces three lines in the NIR band. Their wavelengths are

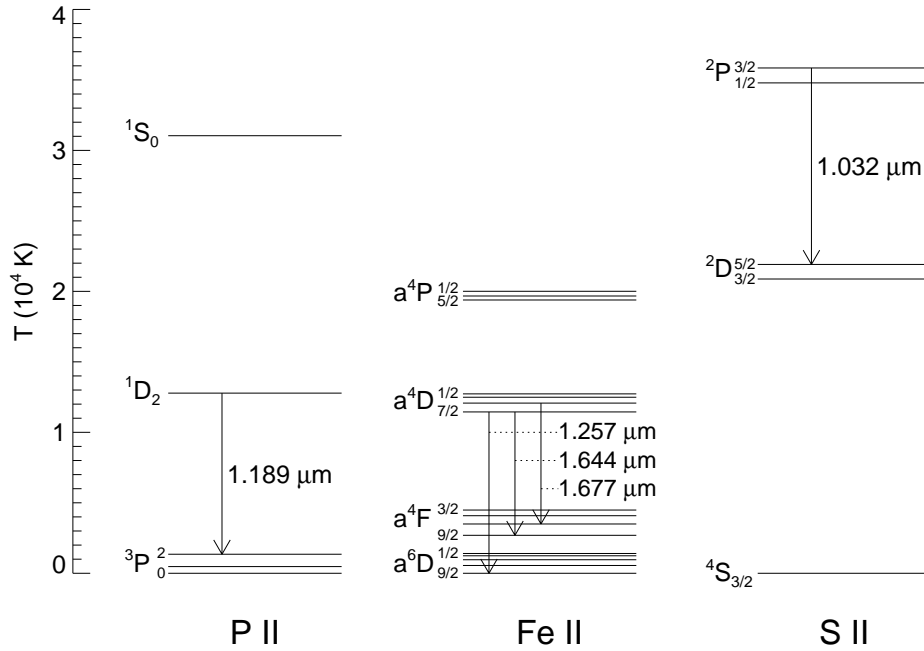


Figure S2: Energy-level diagrams for lowest terms of P II, Fe II, and S II in their ground electronic configurations. The emission lines used in this work are indicated by arrows with their wavelengths (in  $\mu\text{m}$ ) labeled. The energies of upper terms are indicated on the left in temperature scale. The separations of the fine structure levels are magnified for clarity.

1.18861, 1.14713, and  $1.12583 \mu\text{m}$ , and, using the Einstein coefficients in Table S2, their intensity ratios are  $1 : 0.380 : 1.37 \times 10^{-4}$ . We use the dominant  $1.18861 \mu\text{m}$  line in our analysis. Fe II has four ground terms, each of which has closely-spaced 3–5 levels to form a 16 level system. The transitions among these levels produce many lines that appear in the near- to mid-infrared bands (36, 37). The lines to be analyzed in this work are the  $1.25702$ ,  $1.64400$ , and  $1.67734 \mu\text{m}$  lines. The first two lines are the two strongest [Fe II] lines, and as we pointed out in section S1, their intrinsic ratio is constant ( $=1.36$ ).



In Fig. S2, we also show the energy level diagram of S II for completeness. The transitions among the fine structure levels  $^2P_{3/2,1/2}$  and  $^2D_{5/2,3/2}$  produce four adjacent forbidden lines, the strongest of which is the 1.032  $\mu\text{m}$  line (see Fig. S1). Note that the excitation energy of the [S II] 1.032  $\mu\text{m}$  line is significantly higher than those of [P II] and [Fe II] lines, which makes the ratio of [S II] 1.032  $\mu\text{m}$  line to the other lines sensitive to  $T_e$ . In contrast, the excitation energies of the upper states of [P II] 1.189 and [Fe II] 1.257  $\mu\text{m}$  lines are comparable to each other (Table S2), and we can derive a reliable abundance ratio using these two lines.

### Formulation of abundance analysis

The general expression for the flux ( $\text{erg cm}^{-2} \text{s}^{-1}$ ) of an optically thin, ionic spectral line from a knot is given by the integration of surface brightness ( $I_{21}$ ) over the solid angle of the source:

$$F_{21} = \int I_{21} d\Omega = \frac{h\nu_{21}}{4\pi d^2} N_2 A_{21} = \frac{h\nu_{21}}{4\pi d^2} A_{21} f_2 f_{\text{ion}} N_Z \quad (1)$$

where  $N_2$  is the number of ions in the upper state,  $N_Z$  the total number of element Z,  $f_{\text{ion}} (\equiv N_{\text{ion}}/N_Z)$  the fractional ionization of the element,  $f_2 (\equiv N_2/N_{\text{ion}})$  the fractional population of the upper level, and  $d$  the distance to the source. This, together with the line parameters in Table S2, gives the flux ratio of the [P II] 1.189  $\mu\text{m}$  line to the [Fe II] 1.257  $\mu\text{m}$  line

$$\frac{F_{[\text{P II}]1.189}}{F_{[\text{Fe II}]1.257}} = 2.87 \frac{f_{^1D_2, \text{PII}}}{f_{a^4D_{7/2, \text{FeII}}}} \frac{f_{\text{PII}}}{f_{\text{FeII}}} X(\text{P/Fe}), \quad (2)$$

where  $X(\text{P/Fe}) \equiv N_{\text{P}}/N_{\text{Fe}}$  is the abundance ratio that we intend to obtain.

The fractional population of the upper level ( $f_2$ ) can be calculated for given  $n_e$  and  $T_e$  by solving rate equations. When the density is low, collisional excitation and de-excitation are negli-

gible compared to spontaneous radiative transition, and vice versa. For level  $i$ , the critical density can be defined by (38)

$$n_{\text{cr}} \equiv \Sigma A_{ji}(j < i) / \Sigma C_{ij}(j \neq i) \quad (3)$$

where  $\Sigma C_{ij}$  is the collisional (de-)excitation coefficient averaged over a Maxwellian-velocity distribution at temperature  $T_e$ . In terms of the dimensionless collision strength  $\Omega_{21}$ , the excitation and de-excitation coefficients are given by

$$C_{12} = \frac{g_2}{g_1} C_{21} e^{-E_{12}/kT_e}, \quad C_{21} = 8.629 \times 10^{-8} \frac{\Omega_{21}}{g_2} \left( \frac{T_e}{10^4 \text{ K}} \right)^{-1/2}. \quad (4)$$

$\Omega_{21}$  weakly depends on temperature. For Maxwellian-averaged collision strengths for electron-impact excitation, we use the results of (39) and (40) for [P II] and [Fe II] lines, respectively. The critical densities of [P II] and [Fe II] lines are  $3\text{--}5 \times 10^4 \text{ cm}^{-3}$  at  $T_e = 10,000 \text{ K}$  (Table S2).

The fractional ionization cannot be estimated easily. In collisional ionization equilibrium, the P II and Fe II fractions peak near unity at 16,000 and 13,000 K, respectively. The ionization fraction curves are similar with a slight shift in temperature. In shocked gas, however, the ionization curves are affected by time-dependent ionization and photoionization, so that the fractional ionization could be far from the equilibrium value. In the next section, we discuss the structure of shocked SN ejecta, and develop a simple model for the abundance analysis.

### **[P II] and [Fe II] emission from shocked SN ejecta**

The physical structure of shocked SN ejecta has been discussed in several previous studies (41–46). A noticeable characteristic of the shocks propagating into SN ejecta composed of

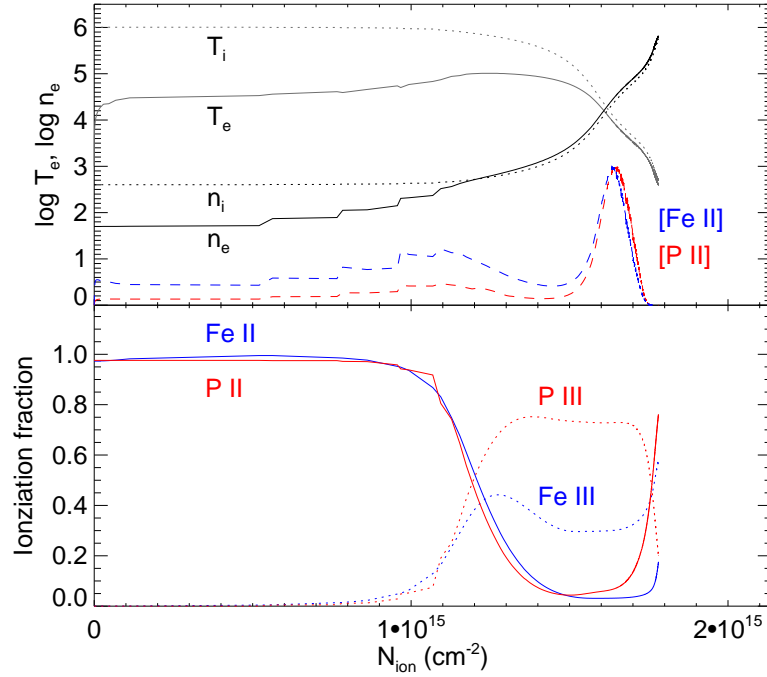


Figure S3: (top) Temperature and density profiles of electrons and ions as a function of swept-up ion-nuclei column density for a  $50 \text{ km s}^{-1}$  shock propagating into an oxygen-enriched SN ejecta of  $n_{\text{ion}} = 100 \text{ cm}^{-3}$ . [P II]  $1.189 \mu\text{m}$  and [Fe II]  $1.257 \mu\text{m}$  line emissivities per ion ( $\text{erg s}^{-1} \text{ sr}^{-1}$ ) are overplotted in a linear scale. (bottom) Ionization fraction profiles of phosphorus and iron. The calculation is done by using a shock code developed for SN ejecta (45, 47, 48) with updated atomic constants for phosphorus.

heavy elements is the strong cooling that occurs before the ions achieve equilibrium ionization states. This is shown in Fig. S3, where we plot the temperature and density profiles (top frame) and ionization fraction profiles of phosphorus and iron (bottom frame) of a ‘typical’ dense SN ejecta knot swept up by a reverse shock. Note that there is an extended “temperature plateau” region where electrons are at temperatures much lower than those of the ions. For the electron gas

in this region, the heating by Coulomb collisions with ions balances with the cooling by the collisional excitation and ionization of the ions. As the electron density increases, the cooling becomes efficient and the electron and ion temperatures drop, which happens in a very narrow region. In the plateau region, both phosphorus and iron atoms are mostly in singly ionized states, ionized by the Galactic background radiation field, i.e.,  $f_{\text{P II}} \approx f_{\text{Fe II}} \approx 1$ . In the cooling region, these fractions decrease as the ions become more highly ionized by electron collisions.

The [P II] and [Fe II] emission lines originate from both the temperature plateau and the cooling regions. The cooling region is very thin and the fractions of the singly ionized ions are low, but these are compensated by the increase in electron density, so that, depending on shock speed, preshock density, and chemical composition, the emission from the cooling region can dominate. In principle, there could be some emission from the preshock region photoionized by the shock radiation (43, 44, 46), but in the Cas A knots the observed high electron densities ( $3 \times 10^3$ – $2 \times 10^5$   $\text{cm}^{-3}$ ; see below) indicate that the observed [P II] and [Fe II] emission lines are mostly from the shocked gas.

In SN ejecta swept-up by a reverse shock, it is likely that a wide range of preshock densities and also a wide range of shock speeds are present (44, 45). We ran a grid of models and have found that, in order to match the observed [Fe II] line ratios, the shock speed should be  $\lesssim 50$   $\text{km s}^{-1}$  and the preshock densities should be  $\gtrsim 100$   $\text{cm}^{-3}$ . For such slow shocks in dense SN ejecta, a simple model where the emitting region is at  $T_e = 10,000$  K and has an uniform density (determined from the [Fe II] line ratios) with  $f_{\text{P II}}/f_{\text{Fe II}} = 1$  yields P/Fe abundance ratio accurate to within

about 30%. For example, the assumed  $X(\text{P}/\text{Fe})$  in the model used in Fig. S3 was 0.10 while it is 0.090 if we apply the simple model to the resulting  $[\text{Fe II}] 1.667/[\text{Fe II}] 1.644$  and  $[\text{P II}] 1.189/[\text{Fe II}] 1.257$   $[\text{Fe II}]$  line ratios. This is because firstly the upper states of the  $[\text{P II}] 1.189 \mu\text{m}$  and  $[\text{Fe II}] 1.257 \mu\text{m}$  lines have comparable excitation energies (12,780 and 11,450 K), so that the level-population ratio ( $f_{1\text{D}_2, \text{P II}}/f_{\text{a}^4\text{D}_{7/2}, \text{Fe II}}$ ) is almost independent of temperature and is mainly a function of electron density  $n_e$ . Secondly their critical densities are comparable ( $3\text{--}5 \times 10^4 \text{ cm}^{-3}$ ) and P and Fe have comparable ionization energies, i.e., 10.49 vs. 7.90 eV for I $\rightarrow$ II and 19.77 vs. 16.19 eV for II $\rightarrow$ III, so that the two lines are emitted from nearly the same spatial volume as we see in Fig. S3. Therefore, we can obtain a reliable estimate of the abundance ratio  $X(\text{P}/\text{Fe})$  from a simple model. Note that this simple model is also applicable for the circumstellar knots of normal chemical composition where the emission is from dense, cooling regions.

Fig. S4 (top) shows the  $[\text{P II}]$  and  $[\text{Fe II}]$  line ratio as a function of electron density at  $T_e = 10,000$  K. We also show the curves for  $T_e = 5,000$  and  $20,000$  K for comparison. The temperature dependence is weak as expected. A great advantage of the broadband NIR spectroscopy is that there exist many  $[\text{Fe II}]$  lines that can be used to derive electron density. One such set is  $[\text{Fe II}] 1.644$  and  $1.677 \mu\text{m}$  lines. Fig. S4 (bottom) shows that the intensity ratio of the two lines is almost independent of temperature. Hence, for a given knot, we can first derive the electron density from  $F_{[\text{Fe II}]1.677}/F_{[\text{Fe II}]1.644}$ , and use this density to estimate  $X(\text{P}/\text{Fe})$ . The mean observed  $F_{[\text{Fe II}]1.677}/F_{[\text{Fe II}]1.644}$  ratio is  $0.167 \pm 0.046$ , corresponding to  $n_e = 2.1 \times 10^4 \text{ cm}^{-3}$ . However, the variations among the knots are large, and electron densities corresponding to  $\pm 2\sigma$  deviations from the mean ( $3.5 \times 10^3\text{--}1.8 \times 10^5 \text{ cm}^{-3}$ ) are marked by dotted lines in Fig. S4. It is worth noting that,

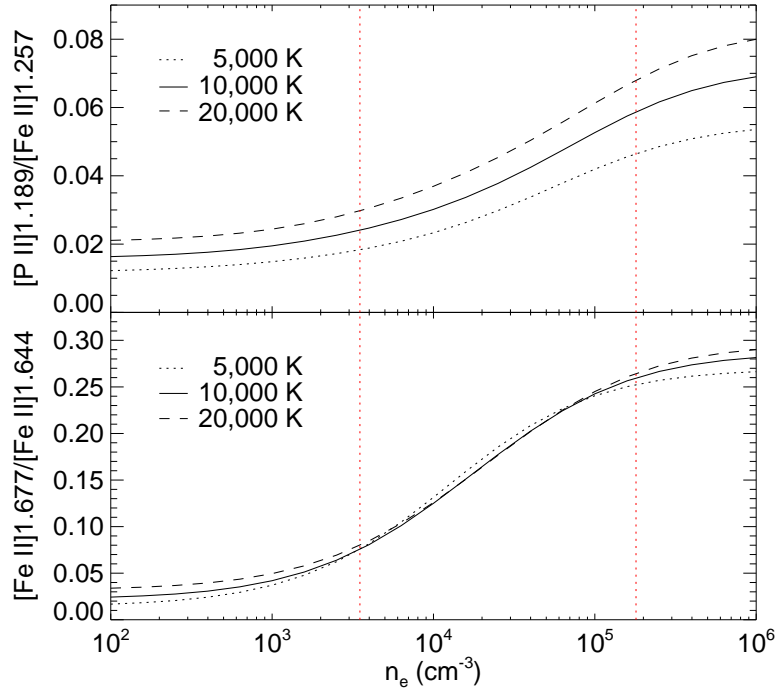


Figure S4: (top) [P II] 1.189/[Fe II] 1.257 line intensity ratio for different temperatures. Note that it assumes  $f_{\text{P II}} = f_{\text{Fe II}}$  and the solar abundance, i.e.,  $N(\text{P})/N(\text{Fe}) = 8.1 \times 10^{-3}[1]$ . The range ( $\pm 2\sigma$ ) of the electron densities of the Cas A knots are marked by dotted lines. (bottom) [Fe II] 1.677/[Fe II] 1.644 line intensity ratio as a function of  $n_e$  for different temperatures.

for the range of the electron densities of the Cas A knots, the flux ratio can be written as

$$\frac{F_{[\text{P II}]1.189}}{F_{[\text{Fe II}]1.257}} = (3 - 7)X(\text{P}/\text{Fe}). \quad (5)$$

29. J. C. Wilson, C. P. Henderson & T. L. Herter, *SPIE*, **5492**, 1295 (2004)

30. T. L. Herter, C. P. Henderson & J. C. Wilson, *SPIE*, **7014**, 30 (2008)

31. J. R. Houck, T. L. Roellig, & J. Van Cleve *et al.*, *SPIE*, **5487**, 62 (2004)

32. J. P. Williams, E. J. de Geus & L. Blitz, *Astrophys. J.*, **428**, 693 (1994)
33. N. C. Deb & A. Hibbert, *Astron. Astrophys.*, **536**, A74 (2011)
34. J. C. Weingartner & B. T. Draine, *Astrophys. J.*, **548**, 296 (2001)
35. S. L. Lumsden & P. J. Puxley, *Mon. Not. R. Astron. Soc.*, **281**, 493 (1996)
36. A. K. Pradhan & S. N. Nahar, *Atomic Astrophysics and Spectroscopy. Cambridge University Press: Cambridge and New York*, (2011)
37. B.-C. Koo, arXiv:1304.3882 (2013)
38. B. T. Draine, *Physics of the Interstellar and Intergalactic Medium. Princeton University Press*, (2011)
39. S. S. Tayal, *Astrophys. J. Suppl. S.*, **150**, 465 (2004)
40. C. A. Ramsbottom, C. E. Hudson, P. H. Norrington & M. P. Scott, *Astron. Astrophys.*, **475**, 765 (2007)
41. H. Itoh, *Pub. Astron. Soc. Japan*, **33**, 121 (1981)
42. H. Itoh, *Pub. Astron. Soc. Japan*, **33**, 521 (1981)
43. M. A. Dopita, Binette, L. & Tuohy, I. R., *Astrophys. J.*, **282**, 142 (1984)
44. R. S. Sutherland & M. A. Dopita, *Astrophys. J.*, **439**, 381 (1995)
45. W. P. Blair, J. A. Morse, J. C. Raymond *et al.*, *Astrophys. J.*, **537**, 667 (2000)

46. D. Docenko & R. A. Sunyaev, *Astron. Astrophys.*, **509**, A59 (2010)
47. J. C. Raymond, *Astrophys. J. Suppl.*, **39**, 1 (1979)
48. D. P. Cox & J. C. Raymond, *Astrophys. J.*, **298**, 651 (1985)
49. C. Mendoza & C. J. Zeppen, *Mon. Not. R. Astron. Soc.*, **199**, 1025 (1982)





Table S1. Flux table for the identified near-infrared knots.

Slit No.	Knot No.	l ["]	$v_{\text{rad}}$ [km/s]	d ["]	$F_{\lambda}$ [ $10^{-15}$ erg s $^{-1}$ cm $^{-2}$ ]					
					[S II] $_{1.032}$	He I $_{1.082}$	[P II] $_{1.189}$	[Fe II] $_{1.257}$	[Fe II] $_{1.644}$	[Fe II] $_{1.677}$
1	1	8.75	1696	118.3	5541(32)	$\leq 46$	719(14)	312(13)	230(4)	55(3)
1	2	3.25	195	104.8	2226(53)	$\leq 53$	253(11)	136(8)	100(3)	8(2)
1	3	5.00	-81	104.6	$\leq 32$	1430(7)	$\leq 13$	290(3)	213(2)	38(2)
1	4	5.50	-2244	103.1	1054(6)	$\leq 8$	62(4)	23(3)	17(3)	$\leq 2$
1	5	5.75	-1100	101.8	1060(10)	$\leq 9$	174(5)	120(3)	88(1)	17(3)
1	6	3.00	-1113	98.3	352(4)	$\leq 4$	55(3)	32(2)	23(1)	6(2)
1	7	5.75	-87	97.3	$\leq 164$	$\leq 79$	$\leq 36$	406(15)	299(6)	15(4)
1	8	3.00	-1252	96.6	636(4)	$\leq 5$	129(3)	48(2)	35(1)	7(3)
2	1	4.50	136	95.9	$\leq 30$	$\leq 27$	$\leq 12$	70(5)	52(3)	4(1)
2	2	5.75	1176	95.6	1738(42)	$\leq 41$	117(24)	49(15)	36(5)	$\leq 10$
2	3	8.00	-702	97.6	1137(15)	$\leq 13$	197(8)	39(6)	29(3)	$\leq 5$
2	4	9.25	798	106.3	1294(26)	$\leq 41$	65(11)	216(9)	159(4)	22(2)
2	5	6.50	1122	106.3	1685(105)	$\leq 61$	120(23)	297(27)	218(8)	$\leq 10$
2	6	3.75	1337	108.4	983(43)	$\leq 27$	29(13)	106(16)	78(4)	5(2)
3	1	6.75	-485	107.8	2282(17)	93(15)	269(11)	252(6)	185(3)	33(2)

Table S1—Continued

Slit No.	Knot No.	l ["]	v <sub>rad</sub> [km/s]	d ["]	F <sub>λ</sub> [10 <sup>-15</sup> erg s <sup>-1</sup> cm <sup>-2</sup> ]					
					[S II] <sub>1.032</sub>	He I <sub>1.082</sub>	[P II] <sub>1.189</sub>	[Fe II] <sub>1.257</sub>	[Fe II] <sub>1.644</sub>	[Fe II] <sub>1.677</sub>
3	2	5.00	-410	105.0	1259(11)	60(10)	116(7)	153(3)	113(2)	21(2)
3	3	7.25	-294	102.3	2960(10)	68(8)	273(8)	460(4)	339(2)	60(2)
3	4	6.50	194	99.6	794(13)	≤40	50(7)	199(5)	146(3)	24(1)
3	5	5.75	270	97.3	184(14)	≤24	≤8	47(5)	35(3)	5(1)
4	1	5.25	1002	95.3	≤396	≤144	≤76	447(56)	329(9)	≤7
4	2	3.75	1272	98.3	1145(41)	272(31)	≤20	240(13)	176(3)	21(2)
4	3	5.75	-513	100.0	≤26	57(10)	≤10	144(5)	106(2)	21(2)
4	4	6.25	859	101.5	5194(28)	≤37	304(14)	444(12)	327(3)	55(3)
4	5	4.00	-8	101.5	≤16	≤14	≤7	98(3)	72(2)	10(1)
4	6	5.75	393	102.0	1626(24)	≤42	134(13)	449(11)	330(4)	49(2)
5	1	5.25	1913	112.3	1465(68)	≤88	85(19)	302(21)	222(5)	33(4)
5	2	5.25	983	112.2	2658(51)	≤36	107(14)	338(14)	249(5)	58(3)
5	3	4.50	1350	112.1	≤91	≤25	≤20	171(13)	125(4)	10(2)
5	4A <sup>a</sup>	6.25	-118	112.2	3596(27)	≤217	94(15)	298(8)	220(3)	42(3)
5	4B <sup>a</sup>	6.25	-118	112.1	≤182	19435(68)	107(15)	1195(8)	880(3)	169(3)

Table S1—Continued

Slit No.	Knot No.	l ["]	v <sub>rad</sub> [km/s]	d ["]	F <sub>λ</sub> [ $10^{-15}$ erg s <sup>-1</sup> cm <sup>-2</sup> ]					
					[S II] <sub>1.032</sub>	He I <sub>1.082</sub>	[P II] <sub>1.189</sub>	[Fe II] <sub>1.257</sub>	[Fe II] <sub>1.644</sub>	[Fe II] <sub>1.677</sub>
5	5	5.25	1544	111.7	1188(31)	≤42	≤27	300(13)	220(3)	36(2)
5	6	4.75	-184	111.4	854(26)	≤120	≤28	165(11)	121(4)	25(3)
5	7	3.75	-494	111.3	536(18)	≤14	≤13	100(6)	73(2)	18(2)
5	8	5.00	605	110.8	1042(52)	≤76	136(22)	418(17)	308(6)	54(3)
5	9	1.75	1579	110.7	882(63)	≤52	≤33	101(16)	74(4)	7(3)
5	10	9.75	-293	110.8	≤98	422(37)	≤40	2564(11)	1887(4)	375(4)
6	1	3.50	1044	114.4	717(12)	≤19	17(6)	102(8)	75(3)	18(2)
6	2	3.25	1391	114.3	1150(21)	≤29	136(12)	215(13)	158(4)	21(2)
6	3	4.25	1913	114.5	833(23)	≤79	123(21)	514(13)	378(4)	61(3)
6	4A <sup>a</sup>	2.75	-159	114.1	≤111	470(25)	≤28	43(7)	32(4)	6(3)
6	4B <sup>a</sup>	2.75	-159	114.0	767(33)	≤55	107(22)	27(8)	20(4)	4(3)
6	5	3.00	1303	114.1	368(34)	≤17	≤16	130(9)	96(3)	15(3)
6	6	6.25	1540	113.7	2600(65)	159(25)	304(20)	565(20)	416(5)	69(3)
6	7	4.50	799	113.2	3858(23)	≤34	247(13)	318(9)	234(4)	48(2)
6	8	2.75	560	112.9	295(20)	≤27	≤35	113(7)	83(3)	13(2)

Table S1—Continued

Slit No.	Knot No.	l ["]	v <sub>rad</sub> [km/s]	d ["]	F <sub>λ</sub> [ $10^{-15}$ erg s <sup>-1</sup> cm <sup>-2</sup> ]					
					[S II] <sub>1.032</sub>	He I <sub>1.082</sub>	[P II] <sub>1.189</sub>	[Fe II] <sub>1.257</sub>	[Fe II] <sub>1.644</sub>	[Fe II] <sub>1.677</sub>
6	9	2.75	528	112.8	≤41	≤23	≤26	143(7)	105(3)	18(2)
6	10	3.50	459	112.8	≤33	≤22	≤20	134(5)	99(2)	17(2)
6	11	6.50	-301	112.9	≤41	129(12)	≤22	295(6)	217(3)	34(2)
6	12	4.25	316	112.9	≤85	≤41	≤31	67(10)	50(4)	7(3)
7	1	3.25	1586	121.8	791(27)	≤34	97(11)	124(8)	91(2)	14(2)
7	2	5.50	-73	123.5	≤23	717(15)	18(6)	240(4)	176(3)	44(1)
7	3	4.00	35	128.5	≤20	731(19)	33(6)	372(3)	274(4)	55(1)
7	4	2.75	75	129.9	≤24	1125(20)	26(6)	276(4)	203(5)	40(1)
7	5	3.25	-78	131.2	≤39	4082(19)	31(9)	331(5)	244(4)	40(2)
8	1	3.25	703	121.9	3294(16)	105(16)	229(8)	96(7)	71(3)	10(2)
8	2	6.00	818	119.2	2161(23)	68(15)	215(9)	182(8)	134(4)	28(2)
8	3	6.25	715	114.9	2013(16)	51(12)	318(9)	210(7)	154(4)	24(2)
8	4	5.25	608	112.0	4789(24)	266(54)	595(11)	235(9)	173(3)	26(2)
8	5	4.50	613	109.4	4484(66)	≤60	567(24)	145(20)	107(6)	11(3)
8	6	4.00	473	108.6	12167(143)	≤140	855(44)	192(28)	141(6)	20(3)

Table S1—Continued

Slit No.	Knot No.	$l$ ["]	$v_{\text{rad}}$ [km/s]	$d$ ["]	$F_{\lambda}$ [ $10^{-15}$ erg s $^{-1}$ cm $^{-2}$ ]					
					[S II] $_{1.032}$	He I $_{1.082}$	[P II] $_{1.189}$	[Fe II] $_{1.257}$	[Fe II] $_{1.644}$	[Fe II] $_{1.677}$
8	7	4.75	640	106.5	4108(67)	$\leq 45$	681(18)	255(16)	188(5)	28(3)
8	8	4.00	122	106.4	331(15)	$\leq 47$	113(8)	103(6)	76(4)	16(2)
8	9	4.00	359	105.0	461(19)	$\leq 31$	210(11)	158(8)	117(3)	22(2)

Note. — Columns 1–5 present slit number, knot number, angular size along the slit ( $l$ ), radial velocity ( $v_{\text{rad}}$ ), and distance ( $d$ ) from the explosion center ( $\alpha = 23^{\text{h}}23^{\text{m}}27^{\text{s}}.77 \pm 0^{\text{s}}.05$ ,  $\delta = 58^{\circ}48'49''.4 \pm 0''.4$  [J2000])[28]. The slit number starts from the top and increases in a counterclockwise direction (Fig. 1 in Report). Note that Slits 5 and 6, represented by relatively short white bars, are located side by side with the former slightly inside. Columns 6–11 present extinction-corrected fluxes of [S II] 1.032, He I 1.082, [P II] 1.189, [Fe II] 1.257, [Fe II] 1.644, and [Fe II] 1.677  $\mu\text{m}$  lines. The intensity ratio of the [Fe II] 1.257 and [Fe II] 1.644  $\mu\text{m}$  lines is constant (1.36) because they share the same upper level (see text). The number in bracket denotes a  $1\sigma$  error of each flux from the Gaussian fit, whereas the upper limits are  $3\sigma$  limits.

<sup>a</sup>These knots in Slits 5 and 6 have been identified as a single knot by *Clumpfind* respectively, but a detailed inspection revealed that each of them are composed of two (A and B) components almost coincident both in space and velocity.

;

Table S2. **Parameters of near-infrared [P II] and [Fe II] lines used in the analysis.**

ion	transition levels		$\lambda$	$A_{21}$	$n_{\text{cr}}$	$T_{\text{ex}}$
	lower	upper	( $\mu\text{m}$ )	( $\text{s}^{-1}$ )	( $\text{cm}^{-3}$ )	(K)
P II	$^3P_2$	$^1D_2$	1.18861	$1.43 \times 10^{-2}$	$5.3 \times 10^4$	12,780
	$^3P_1$	$^1D_2$	1.14713	$5.24 \times 10^{-3}$	$5.3 \times 10^4$	12,780
	$^3P_0$	$^1D_2$	1.12583	$1.85 \times 10^{-6}$	$5.3 \times 10^4$	12,780
Fe II	$a^6D_{9/2}$	$a^4D_{7/2}$	1.25702	$5.27 \times 10^{-3}$	$3.5 \times 10^4$	11,446
	$a^4F_{9/2}$	$a^4D_{7/2}$	1.64400	$5.07 \times 10^{-3}$	$3.5 \times 10^4$	11,446
	$a^4F_{7/2}$	$a^4D_{5/2}$	1.67734	$2.11 \times 10^{-3}$	$3.1 \times 10^4$	12,074

Note. — Columns present ion, lower and upper transition levels, wavelength of the lines ( $\lambda$ ), Einstein  $A$  values, critical density ( $n_{\text{cr}}$ ) at  $T_e = 10,000$  K (see eq. [3] in the text), and excitation energy ( $T_{\text{ex}}$ ) of the upper level. The Einstein  $A$  values are from (49) and (33) for [P II] and [Fe II], respectively.